Investigation of silicon nanoparticles produced by centrifuge chemical vapor deposition for applications in therapy and diagnostics

Lumen, Dave

2021-01

Lumen , D , Wang , S , Mäkilä , E , Imlimthan , S , Sarparanta , M , Rebelo Correia , A M , Haug , C W , Hirvonen , J , Santos , H A , Airaksinen , A , Filtvedt , W & Salonen , J 2021 , ' Investigation of silicon nanoparticles produced by centrifuge chemical vapor deposition for applications in therapy and diagnostics ' , European Journal of Pharmaceutics and Biopharmaceutics , vol. 158 , pp. 254-265 . https://doi.org/10.1016/j.ejpb.2020.11.022

http://hdl.handle.net/10138/329072
https://doi.org/10.1016/j.ejpb.2020.11.022

European Journal of Pharmaceutics and Biopharmaceutics 158 (2021) 254–265

Contents lists available at ScienceDirect

European Journal of Pharmaceutics and Biopharmaceutics

journal homepage: www.elsevier.com/locate/ejpb

Investigation of silicon nanoparticles produced by centrifuge chemical vapor deposition for applications in therapy and diagnostics

Dave Lumen [a,1], Shiqi Wang [b,1], Ermei Mäkilä [c,1], Surachet Imlimthan [a], Mirkka Sarparanta [a], Alexandra Correia [b], Christina Westerveld Haug [d], Jouni Hirvonen [b], Hélder A. Santos [b,e,*], Anu J. Airaksinen [a,*], Werner Filtvedt [d,*], Jarno Salonen [c,*]

[a] Department of Chemistry, Radiochemistry, University of Helsinki, FI-00014 Helsinki, Finland
[b] Drug Research Program, Division of Pharmaceutical Chemistry and Technology, Faculty of Pharmacy, University of Helsinki, FI-00014 Helsinki, Finland
[c] Laboratory of Industrial Physics, Department of Physics and Astronomy, University of Turku, FI-20014 Turku, Finland
[d] Nacamed AS, Askim, Norway
[e] Helsinki Institute of Life Science (HiLIFE), University of Helsinki, FI-00014 Helsinki, Finland

ARTICLE INFO

Keywords:
Porous silicon
Nanoparticles
Production
Toxicity
Biodistribution

ABSTRACT

Porous silicon (PSi) is a biocompatible and biodegradable material, which can be utilized in biomedical applications. It has several favorable properties, which makes it an excellent material for building engineered nanosystems for drug delivery and diagnostic purposes. One significant hurdle for commercial applications of PSi is the lack of industrial scale production of nanosized PSi particles. Here, we report a novel two-step production method for PSi nanoparticles. The method is based on centrifuge chemical vapor deposition (cCVD) of elemental silicon in an industrial scale reactor followed by electrochemical post-processing to porous particles. Physical properties, biocompatibility and *in vivo* biodistribution of the cCVD produced nanoparticles were investigated and compared to PSi nanoparticles conventionally produced from silicon wafers by pulse electrochemical etching. Our results demonstrate that the cCVD production provides PSi nanoparticles with comparable physical and biological quality to the conventional method. This method may circumvent several limitations of the conventional method such as the requirements for high purity monocrystalline silicon substrates as starting material and the material losses during the top-down milling process of the pulse-etched films to porous nanoparticles. However, the electroless etching required for the porosification of cCVD-produced nanoparticles limited control over the pore size, but is amenable for scaling of the production to industrial requirements.

1. Introduction

Porous silicon (PSi) has been investigated as a biocompatible and biodegradable material for biomedical applications already for several decades [1–5]. A large surface area is one of the distinctive properties of all mesoporous materials, however the easily adjustable pore size and versatile possibilities for functionalization of the surface distinguish PSi from other mesoporous materials [5–8]. These favorable properties of PSi have made it an appealing material for pharmaceutical applications and it has been intensively investigated especially as a potential platform for engineered drug delivery systems and for imaging [9–12]. This has led to development of several successful PSi based systems, *e.g.*, for *in vivo* immunogene therapy [13], anti-cancer chemotherapies [14] and brachytherapy [15,16]. The majority of these are still in the pre-clinical development stage, but the brachytherapy agent ^{32}P doped OncoSil™ is currently tested in Phase II clinical trials as a combination treatment with chemotherapeutics for treating pancreatic cancer [17,18]. Due to the recent great progress in development of new PSi based drug delivery systems more candidates can be expected to enter the clinical trials within the coming years.

* Corresponding authors at: Drug Research Program, Division of Pharmaceutical Chemistry and Technology, Faculty of Pharmacy, University of Helsinki, FI-00014 Helsinki, Finland (H.A. Santos). Department of Chemistry, Radiochemistry, University of Helsinki, FI-00014 Helsinki, Finland (A.J. Airaksinen). Nacamed AS, Askim, Norway (W. Filtvedt). Laboratory of Industrial Physics, Department of Physics and Astronomy, University of Turku, FI-20014 Turku, Finland (J. Salonen).
E-mail addresses: helder.santos@helsinki.fi (H.A. Santos), anu.airaksinen@helsinki.fi (A.J. Airaksinen), werner.filtvedt@dynatec.no (W. Filtvedt), jarno.salonen@utu.fi (J. Salonen).
[1] These authors contributed equally.

https://doi.org/10.1016/j.ejpb.2020.11.022
Received 3 May 2020; Received in revised form 23 October 2020; Accepted 27 November 2020
Available online 3 December 2020

Although the porous form of silicon (Si) has been known for decades already, there are still only limited number of methods for processing porous particles from Si in a controlled manner [8]. Especially, the industrial scale production of PSi particles with controlled size, morphology and pore size has been a challenge. All these are critical parameters for pharmaceutical applications. The size, shape, surface charge and surface chemistry of nanoparticles influence recognition of the particles by the immune system of the body and their subsequent removal from the circulation by macrophages [19]. If quickly removed, nanocarrier may not reach to the target tissue, *e.g.*, the tumor and it fails to carry the drug to its target. The pore size, shape and chemistry of the pore wall directly influences drug loading capacity and drug dissolution rate of the material [20]. For porosifying of Si, electrochemical etching has been the dominating technique until the recently introduced methods of metal assisted chemical etching and regenerative electroless etching (ReEtching) [21–23].

Electrochemical etching has exhibited excellent controllability, but it has several drawbacks when large scale production is considered [24]. The method requires expensive high purity monocrystalline Si wafers or wafer-type starting materials. In addition, the method has proven difficult for automation and requires significant amount of manual processing. As a top-down method, the production of PSi particles consists of several different processing steps, which especially when going down into nanoscale increases the material losses and costs of the production. Furthermore, the fine-control of morphology of the top-down produced particles has proven notoriously challenging. Although for microsized PSi particles the fine morphological control has been satisfactorily achieved by using photolithographic methods [25], it is still elusive for production of nanosized particles in large scale [26]. Despite of the intensive research in optimization of the fabrication methods for nanosized PSi particles, the current methods have not yet reached the demands of industrial scale production in terms of reproducible and narrow size distribution and ecological material consumption. So far, this has been one of the biggest stumbling blocks for commercial applications of PSi [27].

In this paper, we introduce a simple two-step production process enabling large scale production of PSi nanoparticles based on centrifuge chemical vapor deposition (cCVD) of elemental Si, followed by electrochemical post-processing to porous particles. Physical properties, biocompatibility and *in vivo* biodistribution of the cCVD produced nanoparticles were investigated and compared to PSi nanoparticles produced from Si wafers by electrochemical etching.

2. Materials and methods

2.1. Materials

PSi particles were fabricated by using a Dynatec reactor (Dynatec Engineering AS, Norway) [28]. Silane was purchased from Praxair Norway AS (Oslo, Norway) at 8 N purity. Reagents for PSi etching and chemical modification were acquired from various sources, such as V_2O_5 (Fisher Scientific Inc.), hydrofluoric acid (HF) 40% and 48%, glacial acetic acid (AcOH), n-pentane, 10-undecenoic acid, all from Merck KGaA, H_2O_2 (30%, VWR) and Si wafers (Siegert Wafer GmbH). Amine PEG_{5k} acetic acid (5000 Da, ≥95% substitution) was purchased from JenKem Technology (Plano, TX, USA). Trypan blue (TB), 1-ethyl-3-(3-dimethylaminopropyl)-carbodiimide (EDC), and N-hydroxysuccinimide (NHS) were purchased from Sigma-Aldrich (St. Louis, MO, USA). Dulbecco's Modified Eagle's Medium (DMEM) and Roswell Park Memorial Institute (RPMI) 1640 were purchased from HyClone™, GE Healthcare Lifesciences (Logan, UT, USA) and fetal bovine serum (FBS) and Versene solution were purchased from Life Technologies Gibco®, USA. CellTiter-Glo® assay was purchased from Promega Corporation, USA. Alexa Fluor™ 488 hydrazide, 4′,6-Diamidino-2-phenylindole dihydrochloride (DAPI), and CellMask™ DeepRed were purchased from Thermo Fisher Scientific (Waltham, MA, USA). Phosphate buffered saline (PBS), non-essential amino acids (NEAA), L-glutamine 200 mM, penicillin (100 IU mL^{-1}), streptomycin (100 mg mL^{-1}) and trypsin (2.5%) were purchased from HyClone™, GE Healthcare Lifesciences (Logan, UT, USA). Triton X-100 was purchased from Merck Millipore (Darmstadt, Germany). All chemicals and solvents for radiolabeling of the PSi NPs were obtained from commercial providers and they were used without further purification. Ultrapure water (18.2 MΩ·cm) was prepared on a Milli-Q Integral 10 water purification system. [^{111}In]$InCl_3$ was purchased from Mallinckrodt Medical B.V. (Petten, The Netherlands).

2.2. Preparation of NPs by centrifuge chemical vapor deposition (UnTHCPSi-CVP)

Silane was loaded into the Dynatec cCVP reactor at 420 °C and set into rotation at a centripetal acceleration exceeding 1000*g*. The reactor was heated to 650 °C initiating the nuclei formation and growth into particles. When reaching the desired size, the Si particles were forced to the wall, from where they were harvested. The harvested material was collected into an inert container and stored under argon until further processed.

The CVP produced Si nanoparticles were initially pre-oxidized under ambient air at 500 °C before annealing in N_2 for 2 h at 900 °C. The annealed nanoparticles were then porosified by regenerative electroless etching [23,29]. The etching was done in a plastic container placed in an ice bath, with the etchant continuously magnetically stirred and sparged with Ar. The etchant composition was a 1:1 (v/v) ratio of 48% HF and AcOH. The primary oxidant V_2O_5 concentration was 20 mM, with the secondary oxidant H_2O_2 added gradually with a syringe pump over the course of the etching. The etching was conducted for 120 min after which the PSi nanoparticles (PSi-CVP) were removed from the etchant using a pressure filtration flask equipped with a membrane filter with a nominal pore size of 200 nm. The filtered particles were washed with copious amounts of ethanol (EtOH), aqueous HCl and finally with *n*-pentane after which the etched PSi-CVP NPs were dried in an oven at 65 °C for at least 1 h.

The etched PSi-CVP NPs were then thermally hydrocarbonized under a continuous 1:1 (v/v) N_2-C_2H_2 flush for 15 min at room temperature (RT) and 15 min at 400 °C. Finally, the thermally hydrocarbonized (TCH) PSi nanoparticles were cooled back to RT under N_2 flush. The NPs were then placed into neat 10-undecenoic acid and heated to 120 °C for 16 h. The COOH-terminated UnTHCPSi-CVP nanoparticles were then washed from the solution by repeated centrifugation and redispersion into EtOH.

2.3. Preparation of UnTHCPSi NPs by pulsed electrochemical etching (UnTHCPSi-PEE)

Boron doped, p^+-type Si(100) wafers of 0.01–0.02 Ω cm resistivity were electrochemically anodized in a 1:1 (v/v) 40% HF-EtOH electrolyte using an etching profile consisting of alternating low and high current density pulses of 50 and 200 mA/cm^2. The obtained multilayer PSi film was detached from the wafer by increasing the current density abruptly to electropolishing region.

The pulse etched films were then thermally hydrocarbonized under 1:1 (v/v) N_2-C_2H_2 flush for 15 min at RT followed by 15 min at 500 °C, and cooled back to RT under N_2. The multilayer THCPSi films were placed into neat 10-undecenoic acid for 16 h at 120 °C. The obtained UnTHCPSi films were then wet-ball-milled in Pulverisette 7 Classic planetary ball mill (Fritsch GmbH, Germany) using ZrO_2 grinding jar and 10 mm balls into nanoparticles in 10 vol-% undecenoic acid-dodecane milling media, with the final size separation done by centrifugation yielding UnTHCPSi-PEE nanoparticles.

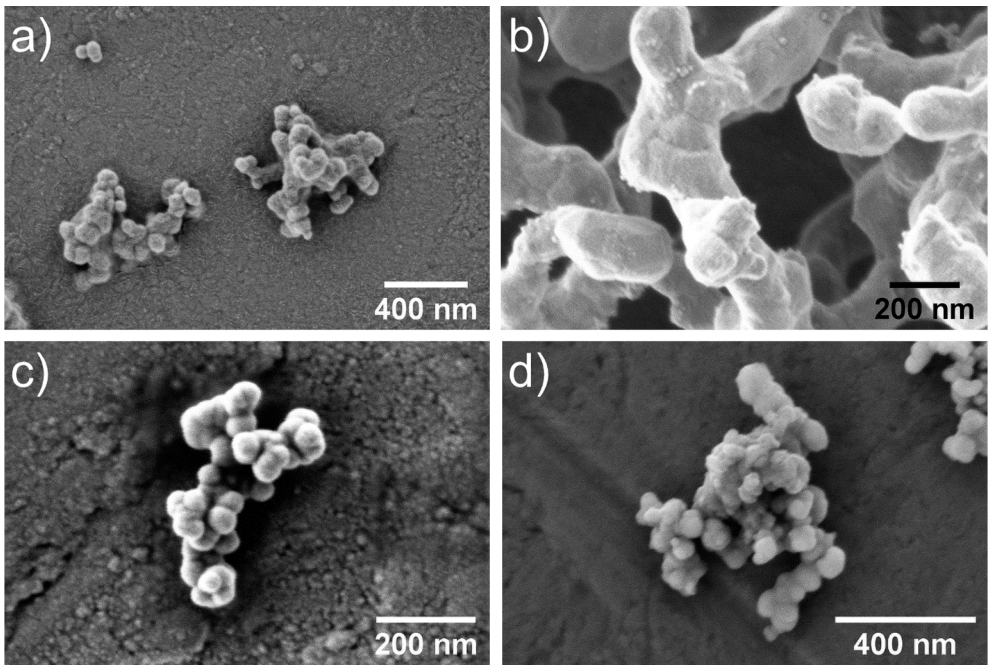

Fig. 1. Secondary electron micrographs of CVD produced Si NPs (a) as produced, (b) directly annealed at 900 °C, (c) oxidized at 500 °C prior to annealing at 900 °C and (d) chemically stabilized into COOH-terminated UnTHCPSi-CVD nanoparticles.

2.4. Preparation of PEGylated PSi nanoparticles and conjugation with Alexa Fluor™ 488 (PEG-CVP, PEG-PEE, Alexa-CVP, Alexa-PEE, Alexa-PEG-CVP and Alexa-PEG-PEE)

UnTHCPSi-CVP or UnTHCPSi-PEE (3 mg) was dispersed in EtOH (1 mL), and tip-sonicated to have a uniform dispersion. EDC (3 μL, 16.9 μmol) and NHS (1.2 mg, 10.4 μmol) was added to the dispersion with vigorous stirring. The reaction was allowed to stir at room temperature for 3 h, which is to activate the carboxylic acid groups. Afterwards, the NHS-activated particles were centrifuged at 16110*g* for 5 min, and washed once with ethanol to remove residual EDC/NHS. Finally, the particles were redispersed in another 1 mL EtOH containing amine PEG_{5k} acetic acid (3 mg, 0.6 μmol). The reaction was allowed to stir for 3 h, and the particles were centrifuged at 16110*g* for 5 min, and washed 3 times with EtOH, water, and EtOH, respectively. The PEG-CVP and PEG-PEE were stored as ethanol dispersion at 4 °C until further use.

For fluorescence labelling, UnTHCPSi-CVP or UnTHCPSi-PEE was first activated by EDC/NHS reaction, same as described above. Then, instead of amine PEG_{5k} acetic acid, 50 μg of Alexa Fluor™ 488 hydrazide (0.09 μmol) in 50 μL water was added and the reaction was protected from light by foil coverage. The resulted particles (Alexa-CVP and Alexa-PEE) were centrifuged at 16110*g* for 5 min, and washed 3 times with EtOH, water, and ethanol, respectively. For the synthesis of Alexa-PEG-CVP, UnTHCPSi-CVP was labelled with Alexa Fluor™ 488 hydrazide and then PEG_{5k}, to make sure that the fluorescence intensity of Alexa-PEG-CVP and Alexa-CVP remained the same.

2.5. Characterization of the nanoparticles

The hydrodynamic size (Z-average) and polydispersity index (PdI) of the PSi samples were determined using dynamic light scattering (DLS; Zetasizer Nano ZS, Malvern Instruments, UK) at RT. The morphology of the different nanoparticles was evaluated by transmission electron microscopy (TEM; Tecnai F12, FEI Company, USA) and field-emission scanning electron microscopy (FE-SEM; Apreo S, Thermo Scientific Inc., The Netherlands). Fourier Transform infrared (FTIR) spectra were recorded on a Bruker Vertex 70 spectrometer using Pike MIRacle attenuated total reflectance accessory (Pike Technologies, USA) and a Bruker Invenio R spectrometer equipped with a PA301 photoacoustic detector (Gasera Oy, Finland).

The crystalline structure of the samples was studied with X-ray diffraction (XRD) measurements using a Panalytical Empyrean diffractometer in θ/θ Bragg-Brentano geometry with Cu Kα radiation and a

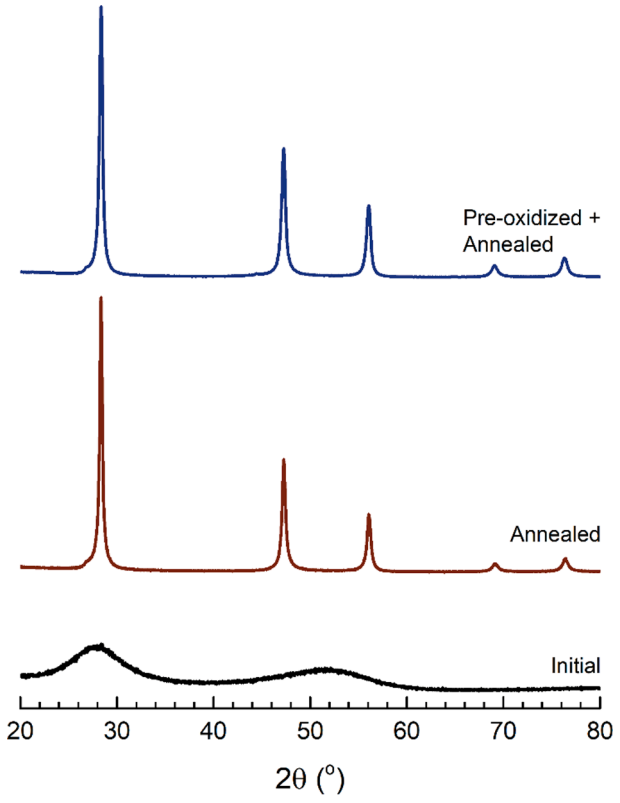

Fig. 2. X-ray diffractograms of the initial CVD produced PSi NPs (CVD NPs), directly annealed nanoparticles and the pre-oxidized, subsequently annealed nanoparticles.

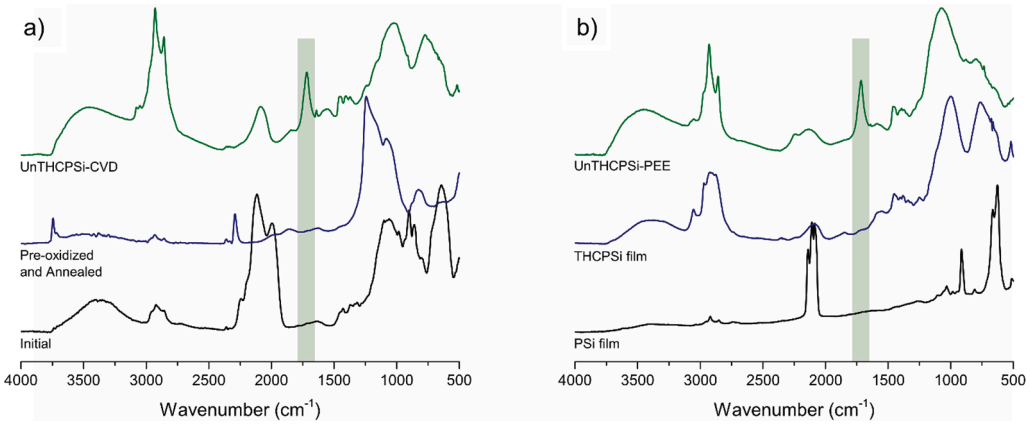

Fig. 3. Photoacoustic FTIR absorbance spectra of the (a) initial CVD-produced Si nanoparticles, the pre-oxidized and annealed nanoparticles and the final, modified COOH-terminated UnTHCPSi-CVD nanoparticles and of the (b) initial anodized PSi film, after thermal hydrocarbonization (THC) and after chemical modification and milling into UnTHCPSi-PEE nanoparticles.

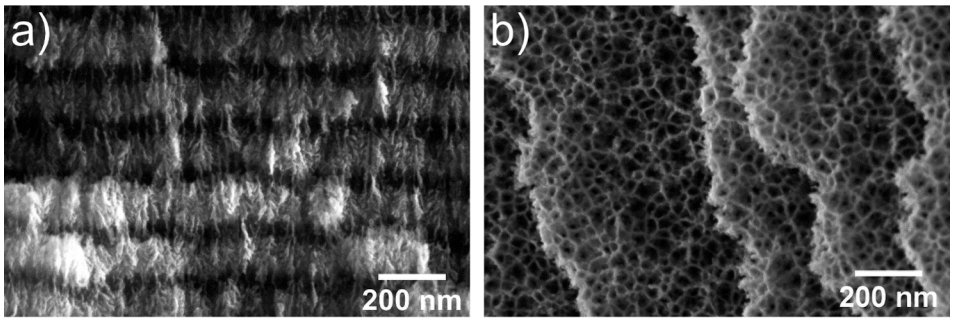

Fig. 4. Secondary electron micrographs of (a) cross-section and (b) top view with some layers removed from a pulse etched multilayer film prior to milling into UnTHCPSi-PEE nanoparticles.

PIXcel^{3D} detector in scanning line mode.

The specific surface area (SSA) and pore volume of the samples was determined with N_2 sorption at −196 °C using TriStar 3000 (Micromeritics Inc., USA). The SSA was calculated using the Brunauer-Emmett-Teller theory and the pore volume by taking the total adsorbed amount at a relative pressure, p/p0 = 0.97 [30]. The average size of the pores was estimated by assuming the pores as cylindrical.

2.6. Cytotoxicity studies

RAW 264.7 macrophage cells were cultured in high glucose (4.5 g L^{-1}) DMEM culture medium, supplemented with 10% FBS, 1% L-glutamine, 1% non-essential amino acids, penicillin (100 IU mL^{-1}) and streptomycin (100 μg mL^{-1}). MDA-MB-231 and 4T1 breast cancer cells were cultured in RPMI 1640 medium supplemented with 10% FBS, penicillin (100 IU mL^{-1}) and streptomycin (100 μg mL^{-1}). All the cells were cultured in the 5% CO_2-incubator at 37 °C, and 95% relative humidity. The culture media were changed every other day. Prior to each test, the cells were passaged using 0.25% (v/v) trypsin EDTA.

The *in vitro* cytotoxicity was performed using a CellTiter-Glo® luminescent cell viability assay. The cells were seeded overnight on a 96-well plate at a density of 1×10^4 cells per well in the cell culture media. Afterwards, PSi NPs at different concentrations were added in the plate. Triton X-100 solution (1% v/v), and cell culture media without any tested materials were used as positive and negative controls, respectively. After 6, 24 and 48 h, the cell viability was detected from the luminescent intensity, which represents the amount of ATP produced by the viable cells. The assay was carried out using Varioskan™ LUX multimode microplate reader (Thermo Fisher Scientific, USA). All samples were tested in four replicates.

2.7. Cell uptake studies

For TEM imaging, cells were seeded on cover-glass slides at a density of 2×10^4 cells per slide. After overnight incubation, UnTHCPSi-PEEs and UnTHCPSi-CVPs were added at a concentration of 100 μg mL^{-1} and incubated for 5 h. Cells without particle treatment were used as control. Then the particles were removed and cells were washed with PBS, before fixation by 4% paraformaldehyde. Then the cells were post-fixed with 1% of osmiumtetroxide, dehydrated with graded series of

Table 1
Average hydrodynamic size, zeta-potential and poly-dispercity index (PdI) of the PSi nanoparticles prepared by CVP and PEE and after different functionalization steps.

	UnTHCPSi-CVP	UnTHCPSi-PEE	PEG-CVP	PEG-PEE
Z-average (nm in water):	206 ± 2	209 ± 1	210 ± 3	193 ± 4
PdI	0.18 ± 0.02	0.22 ± 0.02	0.23 ± 0.01	0.17 ± 0.02
Zeta-potential (mV in water)	−39.1 ± 1.2	−38.1 ± 0.2	−31.7 ± 1.3	−15.5 ± 0.7

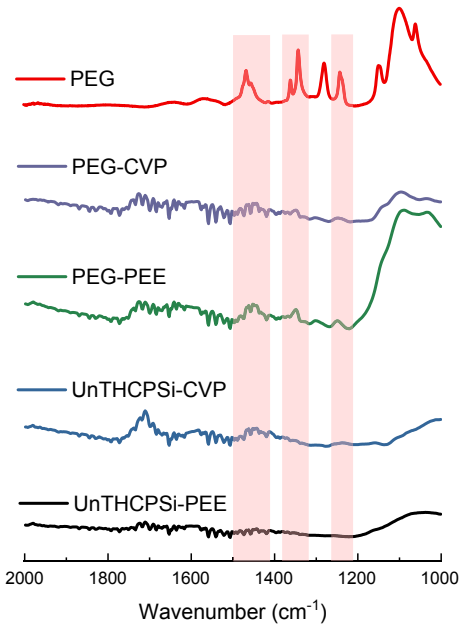

Fig. 5. The FTIR spectrum of PEG and UnTHCPSi before and after PEGylation. The pink shades highlight the typical bands from PEG.

EtOH (70%, 96%, and 100%), incubated with transitional solvent acetone and embedded gradually in Epon. The embedded cells were sectioned at a thickness of 80 nm and attached on a copper grid for TEM imaging (Tecnai F12, FEI Company, USA).

For confocal microscopy, cells were seeded on Lab-Tek® chambered borosilicate coverglass at a cell density of 1.5×10^4 cells per well in cell culture medium. After attachment, the cells were exposed with Alexa Fluor™ 488 labelled PSi nanoparticles at 100 μg mL^{-1} for 5 h. Then the particles were removed and the cells were washed by PBS twice. After washing, the cells were fixed by 4% paraformaldehyde at 37 °C for 10 min, and stained by CellMask™ DeepRed, before imaging by a Leica TCS SP5 II HCS-A confocal microscope (Leica microsystems, Germany). The acquired images were processed by Fiji 1.51 software.

For flow cytometry analysis, cells were seeded in 48-well plates (5×10^4 cells per well). After attachment, the cells were exposed with Alexa Fluor™ 488 labelled PSi NPs at 100 μg mL^{-1}. Cells without particle treatment were used as control. After 24 h treatment, the particles were removed and the cells were washed by PBS twice, before detaching by Versene solution. The detached cells were centrifuged at 317*g* and washed with PBS before analysis on BD Accuri™ C6 Flow Cytometer (BD Biosciences, USA). After flow cytometry analysis, trypan blue (TB) was added to the cell suspension and incubated for 15 min to quench the fluorescence on the cell surface. Then the cells were washed by PBS, and analyzed again by the flow cytometer. The mean fluorescence intensity of each sample (in triplicates) was calculated by BD Accuri™ C6 software (BD Biosciences, USA) and normalized with the control.

2.8. Radiolabelling of the PEG-CVP and PEG-PEE nanoparticles

PEG-CVP and PEG-PEE particles (1.0 mg in EtOH) were centrifuged (10,000 rcf, 5 min) to remove EtOH and redispersed into dimethyl formamide (DMF, 0.6 mL) followed by tip sonication (QSonica, Newtown, CT, U.S.A). 1-[Bis(dimethylamino)methylene]-1H-1,2,3-triazolo [4,5-b]pyridinium 3-oxide hexafluoro-phosphate (HATU) (2 mg, 5.3 μmol) in 50 μL DMF, *N*,*N*-diisopropylethylamine (DIPEA) (1 μL, 5.7 μmol) and (E)-cyclonon-4-en-1-yl (3-(2-(2-(2-aminoethoxy)ethoxy) ethoxy)propyl)carbamate (TCO-PEG_3-NH_2) (3 mg, 8.1 μmol) in 3 μL DMF were added to the particle solution. The reaction was shaken overnight at RT and terminated with centrifugation (10 000 rcf, 5 min) to remove the unreacted reagents, and washed once with EtOH and once with ultrapure water. TCO-functionalized particles were then redispersed back into EtOH for further synthesis.

DOTA-PEG_4-Tz **1** (0.01–0.02 mg, 0.12–0.24 nmol), prepared as described previously [31], was mixed in conical centrifuge tube with 0.2 M ammonium acetate buffer (100–500 μL, pH = 6.8) and [^{111}In] $InCl_3$ (2–80 MBq). The mixture was stirred gently for 30 min at 30 °C and purified by solid phase extraction (Sep-Pak light C-18, Waters Corporation). The C18 cartridge was pretreated with 2 mL of EtOH and 10 mL of ultrapure water. The reaction mixture was loaded to the cartridge, washed with 10 mL ultrapure water and the product, [^{111}In]In-DOTA-PEG_4-Tz ([^{111}In]**1**), was eluted with 20% EtOH in aqueous solution. The TCO functionalized PEG-CVP and PEG-PEE particles, were labeled with

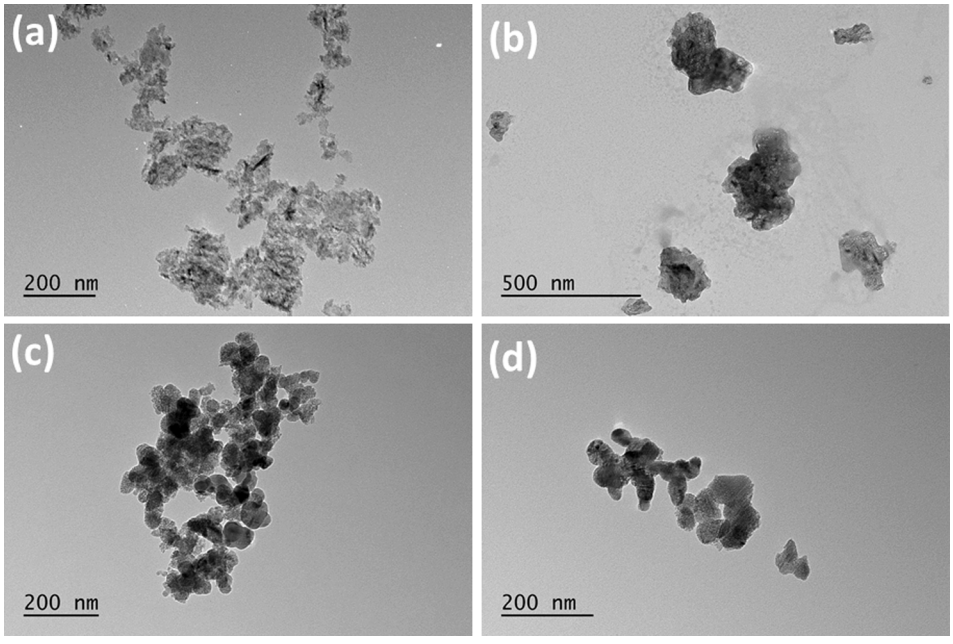

Fig. 6. The TEM images of (a) UnTHCPSi-PEE, (b) PEG-PEE, (c) UnTHCPSi-CVP, and (d) PEG-CVP.

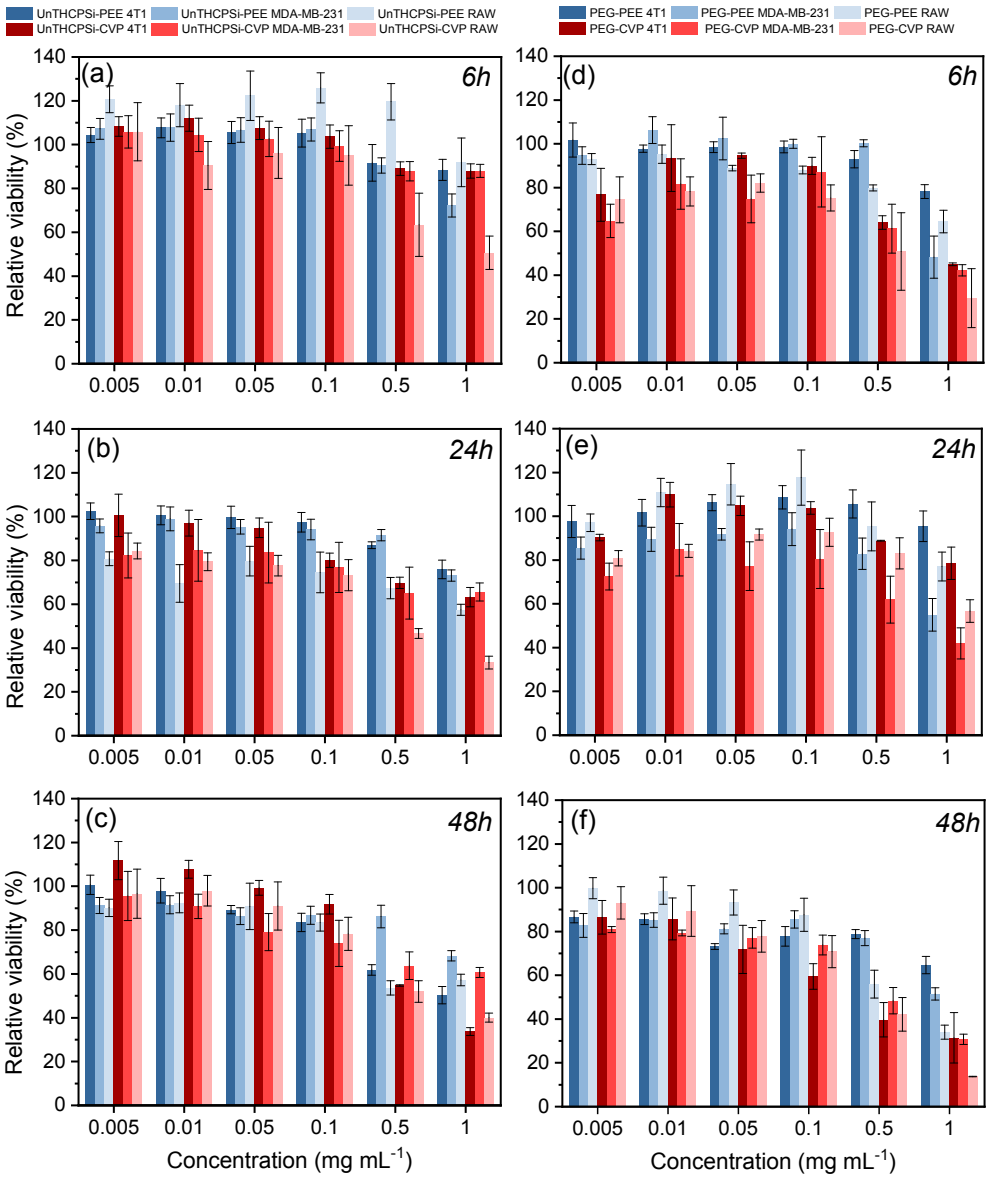

Fig. 7. Cytotoxicity of undecylenic acid (a-c) and PEGylated (d-f) PSi NPs on RAW 264.7, MDA-MB-231 and 4T1 cells for 6, 24, and 48 h.

[^{111}In]In-DOTA-PEG$_4$-Tz ([^{111}In]**1**) for 30 min at 37 °C with constant shaking and purified by repeated centrifugations twice with EtOH and once with water (5 min, 11 900 rcfg). The radiochemical purity of the radiolabeled particles was determined with i-TLC-SA (eluent: 50 mmol EDTA in 0.9% NaCl) and was >98% for the all particle types. Particle size for the radiolabeled particles was measured with Zetasizer Nano ZS (Malvern, Worcestershire, U.K.) in PBS solution.

2.9. Stability of ^{111}In-labeled PEG-CVP and PEG-PEE particles

The *in vitro* radiochemical stability of ^{111}In-radiolabeled NPs (PEG-CVP and PEG-PEE particles) was investigated in PBS (pH = 7.4) and 50% of human plasma in order to confirm that the detected radioactivity originates from the radiolabeled particles instead of a free radionuclide. All assays were carried out in triplicate. Freshly prepared [^{111}In]In-PEG-CVP and [^{111}In]In-PEG-PEE particles (0.3 mg, 2–5 MBq) were added to 1 mL of PBS and 50% of plasma in a protein LoBind microtube (Eppendorf) and incubated at 37 °C under constant shaking. At the predetermined time points 1 h, 2 h and 5 h the nanoparticles were collected by centrifugation and the radioactivity of the pellet and supernatant were separately measured by a dose calibrator (VDC-405, Veenstra Instruments).

2.10. Ex vivo biodistribution studies

All animal experiments were carried out under a project license approved by the National Board of Animal Experimentation in Finland (ESAVI/12132/04.10.07/2017) and in compliance with the respective institutional, national and EU regulations and guidelines. Mice were group-housed in standard polycarbonate cages with aspen bedding and with food (Envigo Teklad Global Diet 2916) and tap water available ad libitum. Environmental conditions of a 12:12 light/dark cycle, temperature of 22 ± 1 °C, and relative humidity of 55 ± 15% were maintained throughout the study.

The *ex vivo* biodistribution studies were carried out in healthy Balb/c female mice purchased from Janvier Laboratories (Saint Berthevin, France), aged 8–10 weeks, weighing 18–22 g (total n = 36). [^{111}In]In-PEG-CVP and [^{111}In]In-PEG-PEE NPs (100 μg) in 200 μL 0.3% Tween in PBS (pH = 7.4), were administered intravenously to the tail vein. The mice were sacrificed at the predetermined time points by CO_2 asphyxiation followed by cervical dislocation. Tissues were collected at 5, 15, 60 and 120 min time points for [^{111}In]In-PEG- CVP and [^{111}In]In-PEG-PEE

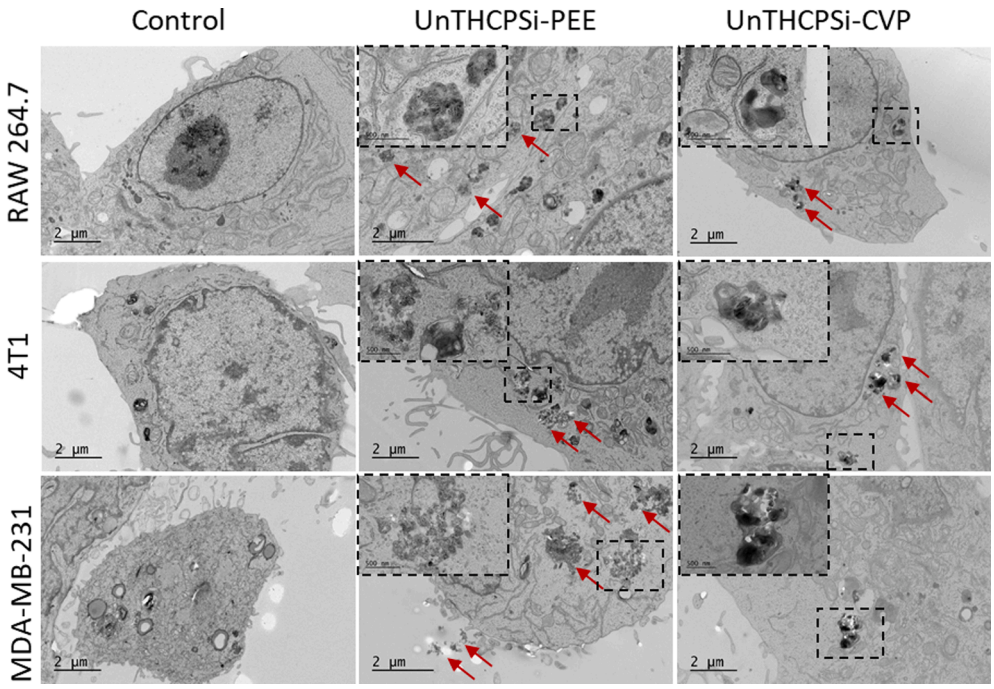

Fig. 8. TEM images of cells after incubation with UnTHCPSi-PEE or UnTHCPSI-CVP, or without particle treatment (control). Red arrows showed the internalized particles, and black rectangle areas are enlarged to show the particles.

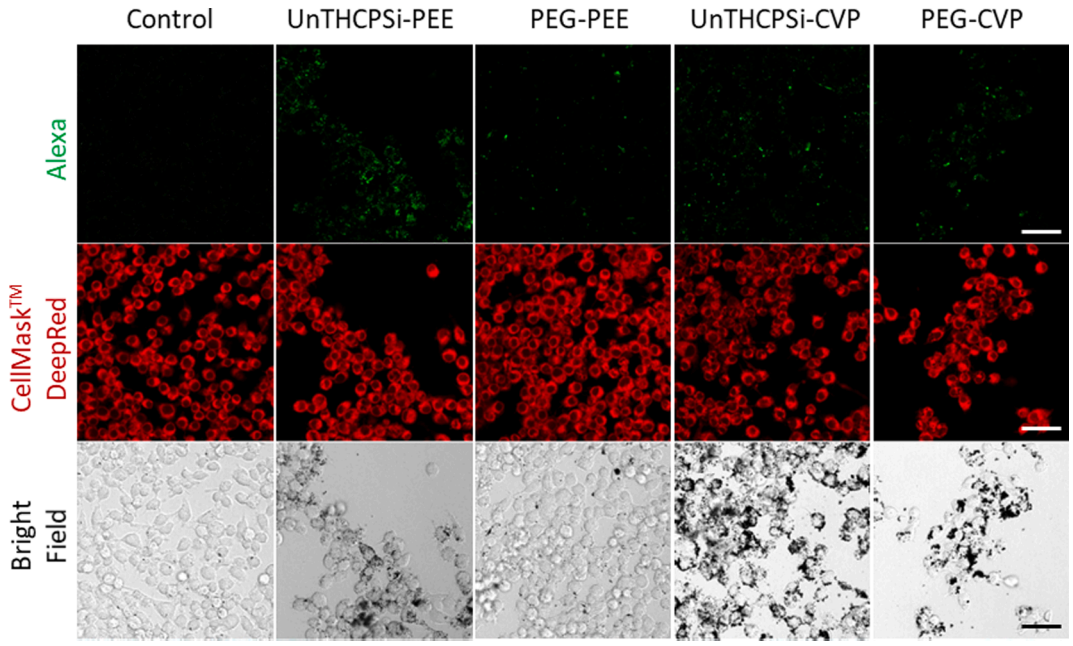

Fig. 9. Confocal microscopy images of RAW 267.4 cells after incubation with UnTHCPSi-PEE, PEG-PEE, UnTHCPSi-CVP, PEG-CVP, or without particle treatment (control). Green channel shows the particles; red channel represents the cell membrane. Scale bar, 50 μm.

particles at 5 and 60 min time points ($n = 4$ at each time point). The circulation half-life of the particles was determined from venous blood samples by collecting a droplet from the tail vein with a needle at 15, 30 and 45 min after administration for both particles. The collected tissue samples were weighted individually, and their radioactivity measured by using an automated gamma counter (Perkin Elmer Life Sciences, Waltham, MA, USA)

3. Results and discussion

3.1. Preparation of PSi nanoparticles by centrifuge chemical vapor deposition and by pulsed electrochemical etching

Chemical vapor deposition (CVD) of Si is based on growth of elemental Si to layers through decomposition of monosilane [32] (Eq. (1)). It is routinely used for production of thin solid high-purity Si films

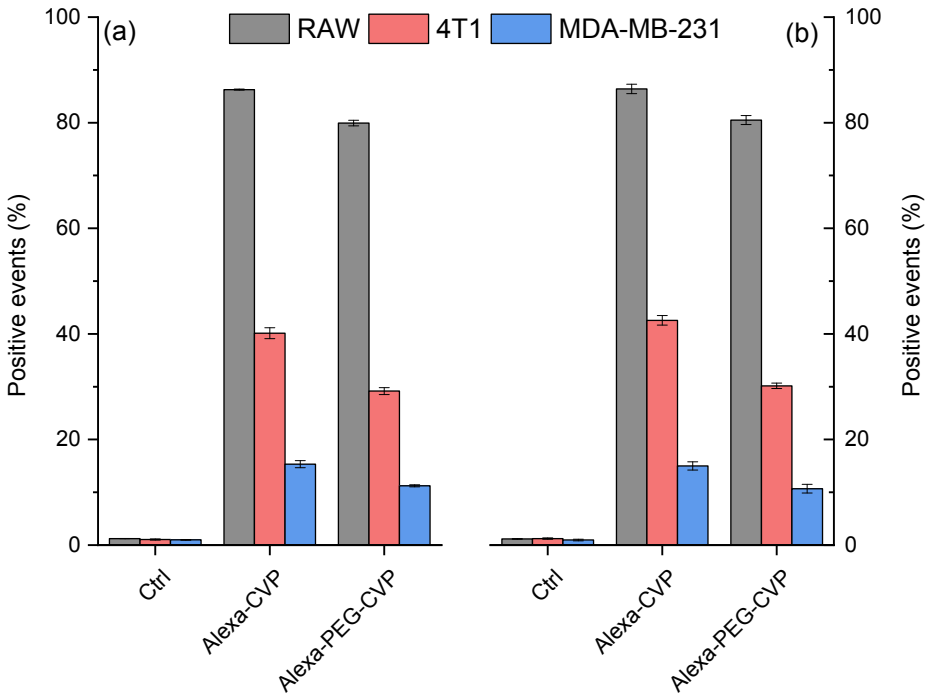

Fig. 10. Flow cytometry quantification of cellular uptake. The positive event percentage of RAW 267.4, 4T1 and MDA-MB-231 cells when incubated 24 h with (a) Alexa-CVP and Alexa-PEG-CVP and (b) after trypan blue (TB) treatment.

for semiconductor industry [33]. For production of PSi nanoparticles, SiO_2 or Si_3N_4 substrates are typically needed for initiating the nucleation process [34,35]. In this work, PSi nanoparticles were produced in a centrifugal chemical vapor deposition reactor (cCVD reactor), in which monosilane decomposition at 420 °C initializes the chain reaction leading to deposition of elemental Si and growth into particles [36].

$$SiH_4 \rightarrow Si + 2H_2 \quad (1)$$

Here, we investigated use of a cCVD reactor for industrial scale production of Si nanoparticles, aiming to controllable and narrow particle size distribution based on separation of the particles with centrifugal forces. The silane was fed into the reactor while the chamber was kept heated and the silane was allowed to nucleate to particles in the chamber, in which the particles continued to scavenge silane and grow [36,37]. Our hypothesis was that as the particles grow, the centripetal force would move them towards the wall within their increasing mass, while the viscous drag would increase by their cross-section. Since the weight scales by r^3 and the cross-section by r^2, the particles are harvested at the same time for each particle as they reach the same r and the centripetal force surpasses the viscous drag agglomeration of the particles during production was observed (Fig. 1a). The primary advantage of the applied cCVD method is the capacity coupled with the particle specifications. The use of rf-decompositon, laser assisted decomposition or plasma assisted decomposition are all based on limiting the growth rate by having a low concentration of silane and thus limit the number of possible molecular collisions within the growth time [38–40]. Since the limiting factor is the available silane, all these methods will have a lower production rate and need more energy per decomposed molecule. Our cCVD method is operated at atmospheric pressure and above, the growth rate is fast and the production rate is high compared to these other methods. Laser ablation is another method where silicon particles are removed from a silicon bulk surface by means of a high energy laser. The method may be effective in producing small particles, but the energy needed and the production rate is limited compared to cCVD.

The process for this particular study utilized a production rate of ca. 660 g/hour, utilizing a silane flow rate of 10 L/min, with a process yield of 97%. The hydrodynamic size of the harvested nanoparticles prior to any further processing was according to DLS measurements in EtOH approximately 220 ± 1 nm. However, some agglomeration of the particles during production was observed (Fig. 1a).

The cCVD reactor produced CVP NPs were amorphous as shown in Fig. 2. Prior to the porosification with regenerative etching, the nanoparticles were crystallized by thermally annealing the particles at 900 °C for 2 h. In order to avoid possible sintering of the particles into larger aggregates, a brief low-temperature oxidation in air at 500 °C was performed prior to the annealing step, preventing further fusion of the primary particles, as observed in Fig. 1b. This pre-oxidation step prevented further aggregation of the primary particles, with the appearance of the particles after both the annealing and final stabilization remaining similar to the initial nanoparticles (Fig. 1c, d). The XRD analysis confirmed the successful crystallization of the NPs (Fig. 2). The broad amorphous halo from the initial particles is replaced after the annealing process with distinct reflections corresponding to polycrystalline Si. Also, the pre-oxidation can be seen to have no discernible effect on crystallization process.

The surface chemistry of the particles, however, showed formation of an oxide layer, as the initial hydrogen termination after production was removed. FTIR measurements done on the initial particles showed a clear presence of different $Si–H_x$ and $O_ySi–H_x$ -groups due to the broad band between 2000 and 2250 cm^{-1}, as shown in Fig. 3. After pre-oxidation and annealing, much of the hydrides were removed except small indications of back-bond oxidized $O_3Si—H$ groups at 2290 cm^{-1}, as well as the presence of silanol groups at 3740 cm^{-1}. In contrast, a broad absorbance band related to Si—O stretching vibrations was observed between 1000 and 1200 cm^{-1}.

The crystallized particles were then porosified with regenerative electroless etching (ReEtching), with reaction conditions adapted for gentle etching due to the initial material being already nanoparticles. As the etching process is initiated by the VO_2^+, both the amount of the oxovanadium ion and the regenerating secondary oxidant was kept low.

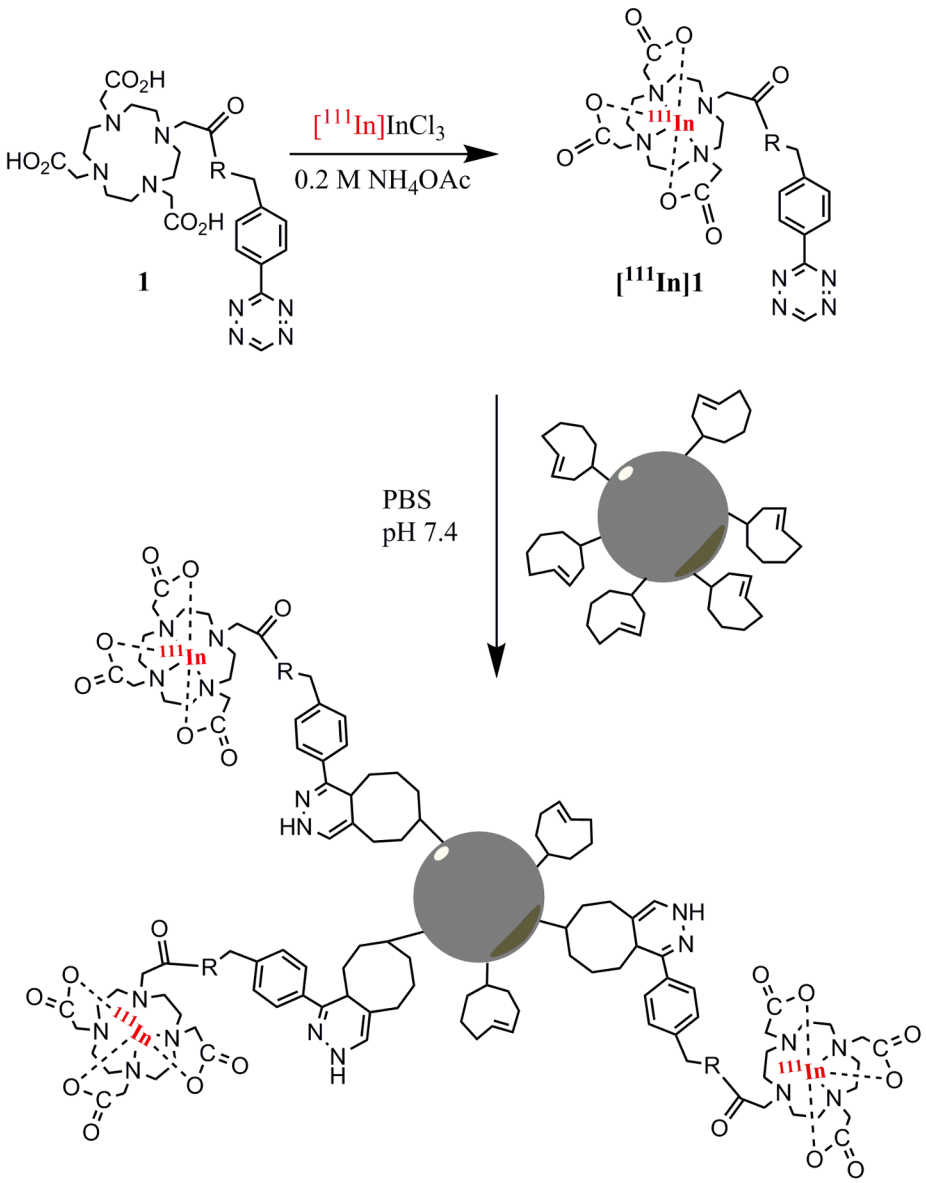

Scheme 1. ^{111}In-radiolabeling of the PEG-PEE and PEG-CVP NPs using the click reaction between *trans*-cyclooctene and [^{111}In]In-DOTA-PEG$_4$-Tz([^{111}In]**1**).

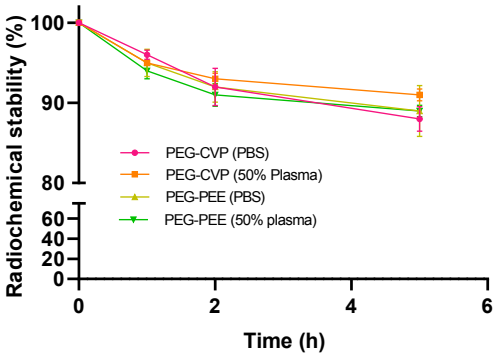

Fig. 11. Radiochemical stability of [^{111}In]In-PEG-CVP and [^{111}In]In-PEG-PEE nanoparticles in PBS and 50% human plasma during 5 h.

The overall amount of added oxidants into the reaction was aimed to provide a clearly substoichiometric oxidant to Si ratio of 0.75 with a process length of 120 min.

After ReEtching, the particle structure became porous and N_2 sorption results indicated the material to have an SSA of over 200 $m^2\ g^{-1}$ with a porosity of ca. 52%. Thermal hydrocarbonization provides aqueous stability and a suitable template for subsequent functionalization, such carboxylic acid termination through thermal addition of 10-undecenoic acid. The initial hydrocarbonization process appeared to cause limited structural collapse of the particles, as the functionalized UnTHCPSi-CVD nanoparticles indicated slight reduction in porosity to 47%, but increase in SSA to nearly 280 $m^2\ g^{-1}$. Analysis of the surface chemistry of the NPs indicated that the functionalization with COOH-groups was successful due to the appearance of a vibration band at 1715 cm^{-1} that can be assigned to carbonyl stretching of the terminal acid group (Fig. 3a).

Anodized PSi nanoparticles with similar surface chemistry were fabricated from Si(1 0 0) wafers. Structurally, the nanoparticles obtained through the pulsed anodization process differ from the CVD-produced and subsequently ReEtched nanoparticles through their pore

morphology. While the ReEtch process produces tortuous pores of 4–6 nm in diameter, the anodization of highly degenerated p^+-type wafers tends to produce larger pores, with diameters of 10–20 nm as can be observed from the micrographs in Fig. 4. After milling into nanoparticles, the SSA and porosity of the nanoparticles were 285 $m^2\ g^{-1}$ and 64%. However, the final surface chemistry after the addition of the COOH-termination is similar to the CVD-produced nanoparticles, as shown in Fig. 4b.

3.2. Surface modification after functionalization with undecylenic acid

An important aim for surface modification of nanoparticles is to improve their biocompatibility and increase *in vivo* circulation half-life and stability. Polyethylene glycol (PEG) is considered as a 'gold standard' for particle/protein surface modification [41] and many PEGylated formulations have been approved by FDA [42]. As a polymer, PEG itself is hydrophilic, biocompatible and non-toxic [42]. It has been demonstrated to induce a 'stealth' effect, which prevents the recognition of particles from the immune system. The PEGylation was achieved by an EDC/NHS coupling reaction between the undecylenic acid group on the UnTHCPSi-CVP and UnTHCPSi-PEE particles and amine group of functionalized PEG [43,44]. After the PEGylation, hydrodynamic size and PdI of the particles remained almost the same, but the negative zeta-potential value decreased, especially for the PEG-PEE (Table 1). FTIR confirmed the successful PEGylation since the typical PEG bands (at 1240 cm^{-1}, 1340 cm^{-1}, 1454 cm^{-1} and 1466 cm^{-1}) were visible in both PEG-PEE and PEG-CVP (Fig. 5).

The morphology of PEGylated particles were characterized by TEM similarly as the unmodified particles. As shown in Fig. 6, the changes in the particle morphology appear to be limited after the PEGylation, suggesting conformal polymer coating of the particles.

3.3. Cytotoxicity studies

The cytotoxicity of the undecylenic acid modified and PEGylated nanoparticles was tested on different mammalian cell lines: RAW 264.7 (mouse macrophage-like cell line), 4T1 (mouse breast cancer cell line) and MDA-MB-231 (human breast cancer cell line, triple negative). As shown in Fig. 7, both UnTHCPSi-PEE and UnTHCPSi-CVP showed higher than 70% cell viability during all the studied time points on 3 cell lines, when the concentration was lower than 0.1 mg mL^{-1}. At 0.5 and 1 mg mL^{-1}, both particles showed significant decreased viability to different extents, especially after the elongation of incubation time to 48 h. Only 33.7% 4T1 and 40.1% RAW 264.7 cells survived after exposure to UnTHCPSi-CVP at 1 mg mL^{-1} for 48 h, while 50.3% 4T1 and 57.2% RAW 264.7 cells survived with 1 mg mL^{-1} UnTHCPSi-PEE after 48 h. The decreased cell viability, quantified by ATP present in living cells using CellTiter-Glo Assay, showed both UnTHCPSi particles caused ATP depletion after exposure to higher concentrations and longer incubation time. Compared with the two cancer cell lines, the toxicity effects were the highest on RAW 264.7 cells, which was probably due to the massive uptake of particles by the macrophages. The higher internalization of particles may cause cell apoptosis, because of reactive oxygen species production and mitochondrial disruption [45]. 4T1 cells were more sensitive to both particles than MDA-MB-231 cells, especially after 48 h-incubation. A similar cell-, concentration-, and time-dependent cytotoxicity trend was observed on PEGylated particles (PEG-CVP and PEG-PEE). Despite the PEGylation, at highest concentrations, 0.5 and 1 mg mL^{-1}, both PEG-CVP and PEG-PEE showed obvious cytotoxicity. PEG-CVP was generally more toxic than PEG-PEE at concentrations above 0.1 mg mL^{-1}, which was consistent with unmodified UnTHCPSi results.

3.4. Cell uptake

The cellular uptake of PSi particles was evaluated on the cell lines indicated above, visualized by both TEM and confocal microscopy. TEM provides fine details about particle internalization pathway, without any labelling. As shown in Fig. 8, RAW 264.7 cells uptake both UnTHCPSi-PEE and UnTHCPSi-CVP nanoparticles. In the zoomed images, the gird-like structure of UnTHCPSi-PEE and the dense sheet-like structure of UnTHCPSi-CVP maintained well after uptake. The particles may have been taken-up as aggregates, since more than one particles were identified in the vesicles. Although similar dark vesicles are shown in the control sample without particle treatment, the staining of these vesicles was uniform without contrast variations inside. The distinct differences between the control and particles treated samples made it clear that the particles were internalized in RAW 264.7 macrophages after treatment. For 4T1 cells, the uptake was also identified, although the internalized particles were less than in RAW 264.7 cells. The internalized particles were packed in irregular vesicles or vesicle aggregates, which suggests that the particle uptake may rely on endocytosis, and the particles were encapsulated in endosome/lysosomes [46,47]. The endosomal/lysosomal entrapment was observed on MDA-MB-231 cells alike.

Confocal microscopy also confirmed the cellular uptake of UnTHCPSi particles, after labelling by Alexa Fluor™ 488. As shown in Fig. 9, all the particles treated samples showed clear spotty green signals in the Alexa channel and dark spots in the bright field channel, suggesting either cell attachment or internalization. Compared with control, the cell morphology and membrane integrity was well maintained after particle treatment, which suggests good biocompatibility. After washing, a large amount of UnTHCPSi-CVP were attached to the cell membrane more than UnTHCPSi-PEE. After PEGylation, both particles showed reduced attachment to cells, confirmed by the fluorescence and bright field images.

Cellular uptake of the non-PEGylated and PEGylated Alexa-CVP and Alexa-CVP particles was quantified by flow cytometry. As shown in Fig. 10, the number of positive events was the highest in RAW 267.4 cells for both non-PEGylated particles, while less positive events were quantified in MDA-MB-231 cells. Consistent with the confocal images shown in Fig. 9, less particle uptake was observed for the PEGylated particles in all investigated cell lines. The TB treatment did not cause any statistically significant difference in the number of the positive events, indicating that the observed signal was contributed by the internalized particles rather than those attached on the cell surface (Fig. 10a, b). The two investigated breast cancer cell lines (4T1 and MDA-MB-231) showed significant difference in the final uptake, in accordance with the cell viability results, in which the MDA-MB-231 cells showed the highest cell viability after long incubation with the particles (Fig. 7).

3.5. ^{111}In-radiolabeling and radiochemical stability of NPs in vivo

PEG-PEE and PEG-CVP NPs were functionalized with *trans*-cyclooctene (TCO) allowing site specific radiolabeling of the particles (RCYs = 72 ± 5% and 66 ± 7%, respectively) by using inverse electron demand Diels-Alder reaction (IEDDA) between TCO and [^{111}In]In-DOTA-PEG$_4$-Tz ([^{111}In]**1**) (Scheme 1). As reported by us previously, the site specific radiolabeling via the IEDDA reaction leads to stable radiolabeling of PSi NPs with indium-111 ($t_{1/2}$ = 2.81 d) and prevents unspecific week coordination of $^{111}In^{3+}$ cation to the negatively charged surface of the particles. Size of the [^{111}In]In-PEG-CVP and [^{111}In]In-PEG-PEE NPs was slightly increased and was 213 ± 3 nm and 268 ± 4 nm, respectively. The radiochemical stability of the ^{111}In-radiolabeled NPs was good (>89% at 5 h time point) both in PBS and plasma (Fig. 11).

3.6. Ex vivo biodistribution

[^{111}In]In-PEG-CVP and [^{111}In]In-PEG-PEE nanoparticles were evaluated in mice order to determine possible differences in their biodistribution. All mice were injected with 100 μg of labeled particles (0.2–0.8 MBq) in 200 μL 0.3% Tween in PBS intravenously into tail vein. Blood samples from the contralateral tail vein were taken at the selected time points to follow the particle residence time in circulation. Mice

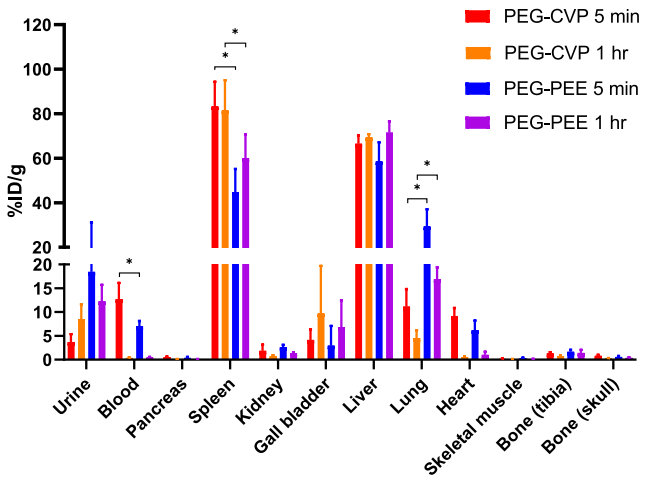

Fig. 12. Biodistribution of [^{111}In]In-PEG-CVP and [^{111}In]In-PEG-PEE nanoparticles at 5 min and 1 h after their intravenous administration to Balb/c mice, represented as injected dose per gram of solid organ or liquid. Statistical significance of the difference (paired *t*-test) between particles for 5 min time point mice: blood $p = 0.019$, spleen $p = 0.0023$ and lung $p = 0.0054$. For the 1 h time point mice: spleen $p = 0.047$ and lung $p = 0.00018$ ($n = 4$ for all groups).

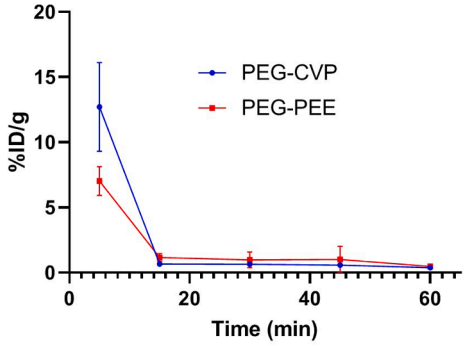

Fig. 13. Radioactivity in blood after intravenous administration of [^{111}In]In-PEG-CVP and [^{111}In]In-PEG-PEE particles to Balb/c mice. Blood samples were collected from the tail vein at 15 min, 30 min and 45 min after administration of the particles ($n = 4$). The results are indicated as %ID/g in blood.

were sacrificed and the selected organs were collected for measurement of their radioactivity concentration with gamma measurements. Both radiolabeled NPs exhibited a typical biodistribution pattern for PSi nanoparticles with high uptakes in the liver (69.4 ± 1.4 %ID/g and 71.5 ± 5.0 %ID/g for [^{111}In]In-PEG-PEE and [^{111}In]In-PEG-CVP, respectively) and spleen (81.5 ± 13.6 %ID/g and 60.0 ± 10.7 %ID/g for [^{111}In]In-PEG-PEE and [^{111}In]In-PEG-CVP, respectively) at 1 h after intravenous administration (Fig. 12). For [^{111}In]In-PEG-PEE, there was significantly higher lung uptake (16.9 ± 2.5 %ID/g at 1 h) when compared to the [^{111}In]In-PEG-CVP particles (4.5 ± 1.7 %ID/g). The lung accumulation is typical for particles with increasing size, but also surface chemistry and shape of nanoparticles may also influence the accumulation [19]. The PEE particles had less negative zeta-potential and slightly bigger size, which both may have contributed to the observed higher accumulation in lungs.

Blood radioactivity levels for [^{111}In]In-PEG-CVP and [^{111}In]In-PEG-PEE NPs were 12.7 ± 3.4 %ID/g and 7.0 ± 1.1 %ID/g at 5 min after their intravenous administration. Despite of the surface PEGylation, the blood circulation time of the particles was short and already after 15 min the radioactivity levels were dropped to 0.7 ± 0.1 %ID/g and 1.2 ± 0.3 %ID/g, respectively (Fig. 13).

4. Conclusions

PSi nanoparticles were successfully produced by using the cCVD reactor. The produced PSi nanoparticles were amorphous and crystallized by thermally annealing the particles at 900 °C prior to the porosification with regenerative etching. Over 50% porosity was achieved, but some structural collapse was observed after hydrocarbonization of the particles lowering the porosity slightly below 50%. Functionalization of the hydrocarbonized nanoparticles with COOH-groups was successful, but the subsequent PEGylation did not yield as high PEG coverage over the cCVD produced particles as achieved for the PSi nanoparticles produced by electrochemical etching. Both particles were equally taken-up by the RAW 264.7 cells. The internalized particles were packed into irregular vesicles or vesicle aggregates, suggesting that the particle uptake may rely on endocytosis, and the particles were encapsulated in endosomes and lysosomes. Not surprisingly the highest cytotoxicity was observed in RAW 264.7 cells, but only significantly at concentrations above 0.1 mg mL^{-1}. PEGylation decreased macrophage uptake for both particle types, but did not have significant influence on the observed cytotoxicity of the particles at high concentrations. As expected based on the *in vitro* RAW 264.7 cell uptake, both PEGylated nanoparticle types were equally recognized by the immune system *in vivo* and quickly sequestrated from blood by the liver and spleen. Further optimization is needed for improving stealth properties of the particles with more efficient masking against recognition by the macrophages.

Overall, the cCVD method provides an alternative method to the fabrication of PSi nanoparticles along to the top-down approach utilized in the pulsed anodization route. The new route circumvents the limitations placed by the utilization of high purity monocrystalline wafers and their subsequent anodization and milling. The electroless etching required for the porosification of cCVD-produced nanoparticles limits control over the pore size, but allows far greater flexibility in the scaling of the production to industrial requirements. However, further optimization of the cCVD method is needed for minimizing agglomeration of the particles in the chamber. This may be achieved by controlling the particle growth speed and the surface chemistry of the particles for reducing probability of particles to adhere when they collide.

5. Funding sources

The project was funded as a joined funding of the Norwegian Research Council and Nacamed AS from the Nano2021 program (decision no. 281906). Additionally, the Academy of Finland (decision no. 320102) and the Finnish Cultural Foundation are acknowledged for financial support.

6. Notes

The authors declare the following competing financial interests: C.W. H. is member of the board of Nacamed AS and W.F. is R&D director and founder of Nacamed AS.

Declaration of Competing Interest

The authors declare that they have no known competing financial interests or personal relationships that could have appeared to influence the work reported in this paper.

Acknowledgement

Helsinki University HiLIFE and Biocenter Finland core facilities: Electron Microscopy Unit for TEM and the Light Microscopy Unit of the Institute of Biotechnology for the confocal microscope are acknowledged.

References

[1] D.J. Savage, et al., Porous silicon advances in drug delivery and immunotherapy, Curr. Opin. Pharmacol. 13 (5) (2013) 834–841.
[2] E.J. Anglin, et al., Porous silicon in drug delivery devices and materials, Adv. Drug Deliv. Rev. 60 (11) (2008) 1266–1277.
[3] N.H. Voelcker, et al., The biocompatibility of porous silicon in tissues of the eye, Biomaterials 30 (15) (2009) 2873–2880.
[4] H.A. Santos, Porous Silicon for Biomedical Applications, Woodhead Publishing, 2014.
[5] L.T. Canham, Bioactive silicon structure fabrication through nanoetching techniques, Adv. Mater. 7 (12) (1995) 1033–1037.
[6] J. Salonen, V.-P. Lehto, Fabrication and chemical surface modification of mesoporous silicon for biomedical applications, Chem. Eng. J. 137 (1) (2008) 162–172.
[7] C. Chiappini, et al., Tailored porous silicon microparticles: fabrication and properties, ChemPhysChem 11 (5) (2010) 1029–1035.
[8] L. Canham, Handbook of Porous Silicon, Springer, 2014.
[9] H.A. Santos, et al., Multifunctional porous silicon for therapeutic drug delivery and imaging, Curr. Drug Discov. Technol. 8 (3) (2011) 228–249.
[10] H.A. Santos, J. Salonen, L.M. Bimbo, Porous silicon for drug delivery, in: Encyclopedia of Metalloproteins, Springer, 2013, pp. 1773–1781.
[11] D.-X. Zhang, et al., Porous silicon nanomaterials: recent advances in surface engineering for controlled drug-delivery applications, Nanomedicine 14 (24) (2019) 3213–3230.
[12] Karaman Didem Şen, M.P. Sarparanta, Jessica M. Rosenholm, Anu J. Airaksinen, Multimodality imaging of silica and silicon materials in vivo, Adv. Mater. (2018) 1703651.
[13] B. Kim, et al., Immunogene therapy with fusogenic nanoparticles modulates macrophage response to Staphylococcus aureus, Nat. Commun. 9 (1) (2018) 1–13.
[14] T. Yong, et al., Tumor exosome-based nanoparticles are efficient drug carriers for chemotherapy, Nat. Commun. 10 (1) (2019) 1–16.
[15] A.S.-W. Goh, et al., A novel approach to brachytherapy in hepatocellular carcinoma using a phosphorous32 (32P) brachytherapy delivery device—a first-in-man study, Int. J. Radiat. Oncol. Biol. Phys. 67 (3) (2007) 786–792.
[16] K. Zhang, et al., Complete tumor response following intratumoral 32P BioSilicon on human hepatocellular and pancreatic carcinoma xenografts in nude mice, Clin. Cancer Res. 11 (20) (2005) 7532–7537.
[17] P.J. Ross, et al., PanCO: An open-label, single-arm pilot study of phosphorus-32 (P-32; Oncosil) microparticles in patients with unresectable locally advanced pancreatic adenocarcinoma (LAPC) in combination with FOLFIRINOX or gemcitabine+ nab-paclitaxel (GNP) chemotherapies, Am. Soc. Clin. Oncol. (2019), 4125–4125.
[18] M.S. Bhutani, et al., An open-label, single-arm pilot study of EUS-guided brachytherapy with phosphorus-32 microparticles in combination with gemcitabine+/-nab-paclitaxel in unresectable locally advanced pancreatic cancer (OncoPaC-1): Technical details and study protocol, Endosc. Ultrasound 9 (1) (2020) 24.
[19] E. Blanco, H. Shen, M. Ferrari, Principles of nanoparticle design for overcoming biological barriers to drug delivery, Nat. Biotechnol. 33 (9) (2015) 941–951.
[20] T. Limnell, et al., Surface chemistry and pore size affect carrier properties of mesoporous silicon microparticles, Int. J. Pharm. 343 (1) (2007) 141–147.
[21] Z. GX, et al., Porous silicon: morphology and formation mechanisms, in: Modern Aspects of Electrochemistry, Springer US, Boston, MA, 2006, pp. 65–133.
[22] X. Li, P. Bohn, Metal-assisted chemical etching in HF/H 2 O 2 produces porous silicon, Appl. Phys. Lett. 77 (16) (2000) 2572–2574.
[23] E. Mäkilä, et al., Hierarchical nanostructuring of porous silicon with electrochemical and regenerative electroless etching, ACS Nano 13 (11) (2019) 13056–13064.
[24] H. Kim, N. Cho, Morphological and nanostructural features of porous silicon prepared by electrochemical etching, Nanoscale Res. Lett. 7 (2012) 408.
[25] B. Godin, et al., Discoidal porous silicon particles: fabrication and biodistribution in breast cancer bearing mice, Adv. Funct. Mater. 22 (20) (2012) 4225–4235.
[26] H. Alhmoud, et al., Porous silicon nanodiscs for targeted drug delivery, Adv. Funct. Mater. 25 (7) (2015) 1137–1145.
[27] P.A. Kulyavtsev, R.P. Spencer, Drug delivery via porous silicon: a focused patent review, Pharm. Pat. Anal. 6 (2) (2017) 77–85.
[28] J. Filtvedt, W.O. Filtvedt, Reactor and method for production of silicon, WO2010136529A1 (2010).
[29] K.W. Kolasinski, et al., Regenerative electroless etching of silicon, Angew. Chem. 129 (2) (2017) 639–642.
[30] M. Thommes, et al., Physisorption of gases, with special reference to the evaluation of surface area and pore size distribution (IUPAC Technical Report), Pure Appl. Chem. 87 (9–10) (2015) 1051–1069.
[31] D. Lumen, et al., Site-specific ^{111}In-radiolabeling of dual-PEGylated porous silicon nanoparticles and their in vivo evaluation in murine 4T1 breast cancer model, Pharmaceutics 11 (12) (2019) 686.
[32] J.M. Jasinski, S.M. Gates, Silicon chemical vapor deposition one step at a time: fundamental studies of silicon hydride chemistry, Acc. Chem. Res. 24 (1) (1991) 9–15.
[33] Rinaldi, et al., CVD technologies for silicon: a quick survey, in: Semiconductors and Semimetals, vol. 72, 2001, pp. 1–50.
[34] W.T. Leach, J.-H. Zhu, J.G. Ekerdt, Thermal desorption effects in chemical vapor deposition of silicon nanoparticles, J. Cryst. Growth 243 (1) (2002) 30–40.
[35] T. Baron, et al., Nucleation control of CVD growth silicon nanocrystals for quantum devices, Microelectron. Eng. 61 (2002) 511–515.
[36] W. Filtvedt, et al., Chemical vapor deposition of silicon from silane: Review of growth mechanisms and modeling/scaleup of fluidized bed reactors, Sol. Energy Mater. 107 (2012) 188–200.
[37] M. Vazquez-Pufleau, M. Yamane, Relative kinetics of nucleation and condensation of silane pyrolysis in a helium atmosphere provide mechanistic insight in the initial stages of particle formation and growth, Chem. Eng. Sci. 211 (2020) 115230.
[38] P. Blandin, et al., Femtosecond laser fragmentation from water-dispersed microcolloids: toward fast controllable growth of ultrapure Si-based nanomaterials for biological applications, J. Mater. Chem. B 1 (19) (2013) 2489–2495.
[39] V.M. Fomin, V.Y. Timoshenko, Spin-dependent phenomena in semiconductor micro-and nanoparticles for biomedical applications, Appl. Sci. 10 (14) (2020) 4992.
[40] L. Mangolini, E. Thimsen, U. Kortshagen, High-yield plasma synthesis of luminescent silicon nanocrystals, Nano Lett. 5 (4) (2005) 655–659.
[41] Y. Qi, A. Chilkoti, Protein–polymer conjugation—moving beyond PEGylation, Curr. Opin. Chem. Biol. 28 (2015) 181–193.
[42] M. Roberts, M. Bentley, J. Harris, Chemistry for peptide and protein PEGylation, Adv. Drug Deliv. Rev. 54 (4) (2002) 459–476.
[43] M.P. Ferreira, et al., In vitro and in vivo assessment of heart-homing porous silicon nanoparticles, Biomaterials 94 (2016) 93–104.
[44] C.-F. Wang, et al., Multifunctional porous silicon nanoparticles for cancer theranostics, Biomaterials 48 (2015) 108–118.
[45] H.A. Santos, et al., In vitro cytotoxicity of porous silicon microparticles: effect of the particle concentration, surface chemistry and size, Acta Biomater. 6 (7) (2010) 2721–2731.
[46] L.M. Bimbo, et al., Drug permeation across intestinal epithelial cells using porous silicon nanoparticles, Biomaterials 32 (10) (2011) 2625–2633.
[47] M.-A. Shahbazi, et al., A prospective cancer chemo-immunotherapy approach mediated by synergistic CD326 targeted porous silicon nanovectors, Nano Res. 8 (5) (2015) 1505–1521.